Available online at www.sciencedirect.com
ScienceDirect
International Journal of Multiphase Flow 34 (2008) 393–407
International Journal of Multiphase Flow
www.elsevier.com/locate/ijmulflow

A numerical study of an annular liquid jet in a compressible gas medium

George A. Siamas, Xi Jiang *, Luiz C. Wrobel

Mechanical Engineering, School of Engineering and Design, Brunel University, Uxbridge UB8 3PH, UK

Received 9 March 2007; received in revised form 10 September 2007

Abstract

An annular liquid jet in a compressible gas medium has been examined using an Eulerian approach with mixed-fluid treatment. The governing equations have been solved by using highly accurate numerical methods. An adapted volume of fluid method combined with a continuum surface force model was used to capture the gas–liquid interface dynamics. The numerical simulations showed the existence of a recirculation zone adjacent to the nozzle exit and unsteady large vortical structures at downstream locations, which lead to significant velocity reversals in the flow field. It was found that the annular jet flow is highly unstable because of the existence of two adjacent shear layers in the annular configuration. The large vortical structures developed naturally in the flow field without external perturbations. Surface tension tends to promote the Kelvin–Helmholtz instability and the development of vortical structures that leads to an increased liquid dispersion. A decrease in the liquid sheet thickness resulted in a reduced liquid dispersion. It was identified that the liquid-to-gas density and viscosity ratios have opposite effects on the flow field with the reduced liquid-to-gas density ratio demoting the instability and the reduced liquid-to-gas viscosity ratio promoting the instability characteristics.

Keywords: Annular jet; Direct numerical simulation; Gas; Liquid; Surface tension; Two-phase flow; Vortical structure

1. Introduction

Annular jets have many applications such as in air-blasted atomisers in gas turbine combustors for aircraft propulsion and in annular orifice injectors and hollow-cone sprays in combustion engines (e.g. Adzic et al., 2001; Lozano et al., 2001, 2005; Stiesch, 2003). An annular liquid jet present in a gas medium is a complex multiphase flow problem. Detailed studies on the flow instabilities and liquid breakup phenomena of annular liquid jets are very scarce. Many of the existing studies, such as those by Choi and Lee (2005), Ibrahim and McKinney (2006) and Lasheras et al. (1998), were focused on experimental visualisations and simplified mathematical models, which are insufficient to reveal and describe the complex details of liquid breakup and atomisation. Although useful insights have been obtained, including the inherently unstable behaviour of the annular jet (Lin and Reitz, 1998; Ramamurthi and Tharakan, 1998; Mehring and Sirignano, 2000), a detailed knowledge on the physics of such flows is still not available.

In many applications of annular jets, the flow is high-speed and the gas phase is compressible such as in the fuel injection and spray combustion processes in propulsion systems and automotive industry. The interactions between the compressible gas phase and the liquid can occur in different ways involving various fluid dynamic factors. Annular jets have some distinctive features compared to round jets. A prominent fluid dynamic characteristic of annular jets is the presence of two adjacent circular shear layers near the jet nozzle exit, in comparison to one such shear layer in round jets. Typical features of annular jets include the existence of a recirculation zone very close to the jet nozzle exit (Del Taglia et al., 2004; Sheen et al., 1996), which is absent in round jets. Due to the existence of the recirculation zone, annular jets have the well known "bell shape" near the nozzle exit at upstream locations (Ibrahim and McKinney, 2006), after which the flow collapses as the flow progresses to downstream locations.

* Corresponding author. Tel.: +44 1895 266685; fax: +44 1895 256392.
E-mail address: Xi.Jiang@brunel.ac.uk (X. Jiang).

0301-9322/$ - see front matter © 2007 Elsevier Ltd. All rights reserved.
doi:10.1016/j.ijmultiphaseflow.2007.10.010

The breakup of liquid jets and sheets, including that of annular jets, is an essential stage in the atomisation and spray processes, but there is insufficient knowledge on the real physics of atomisation and the exact mechanisms of liquid breakup still remain unclear (De Villiers et al., 2004). It is difficult to fully understand the breakup process using theoretical and/or experimental approaches because of the complex fluid dynamic behaviour of liquid jets in a compressible gas environment, involving mixing at a broad range of time and length scales and complex interaction and coupling between the two phases.

Within the context of numerical studies of gas–liquid two-phase flow phenomena, the traditional Reynolds-averaged Navier–Stokes (RANS) modelling approach could lead to poor predictions of highly unsteady and complex flow phenomena involving vortical structures due to the intrinsic time- or ensemble-averaging of governing equations. Large-eddy simulation can be used to overcome the problems associated with the averaging involved in RANS approach but it may not be sufficient to understand the detailed mechanisms in a high-speed multiphase flow, since small scales still need to be modelled. In this context, direct numerical simulation (DNS) can be a very powerful tool that not only leads to a better understanding of the fluid mechanics involved, but also provides useful databases for the potential development of physical models for liquid breakup and atomisation in gas environments.

Many studies have been performed using DNS to simulate the interface changes and turbulence in two-phase environments (e.g. Banerjee et al., 2004; Fulgosi et al., 2003; Lombardi et al., 1995) but the two phases were divided into two single-phase sub-domains with the gas flow considered as incompressible. These efforts focused on the surface behaviour and the two phases were treated as separate phases. There are a few studies referring to simulations of spatially developing liquid films. Richards and Lenhoff (1995) simulated a liquid–liquid flow by injecting *N*-heptane jet into water and compared the results with experimental data. Albina and Peric (2000) investigated the Rayleigh breakup and atomisation and obtained good agreement with experimental results. Leboissetier and Zaleski (2001) simulated a diesel spray injection and evaluated spray angles. Klein (2005) performed a three-dimensional, spatially developed DNS of a liquid sheet exhausting into a gaseous incompressible atmosphere under moderate Reynolds number. However, the gas compressibility has largely been ignored in the existing gas–liquid two-phase flow simulations. Furthermore, the effects of liquid sheet thickness, liquid surface tension, and the density and viscosity ratios of the two phases on the flow development have not been extensively examined through advanced numerical simulation techniques.

This study aims at a better understanding on the flow physics of annular liquid jets in compressible gas environments by providing detailed information on the gas–liquid two-phase flow field by solving the governing equations to a high degree of accuracy. The DNS approach used is able to resolve the detailed flow structures in the two-phase flow field. The direct computation is achieved by solving the axisymmetric Navier–Stokes equations with the inclusion of the effect of surface tension. Many studies can be found in the literature concerning the surface tension effect in free-surface flows (e.g. Hou et al., 2001; Nie, 2001; Rangel and Sirignano, 1991; Zhang et al., 2001) but none of them combined DNS with a compressible gas formulation in an annular configuration. In this study, an adapted volume of fluid and continuum surface force techniques have been used to study the gas–liquid interface dynamics. Herein, the gas is assumed to be fully compressible, while the liquid is taken to be incompressible due to its infinitesimal compressibility. This study investigates the effects of liquid sheet thickness, surface tension, and liquid-to-gas density and viscosity ratios on the fluid dynamics of an annular liquid jet in a gas environment. In the following sections, governing equations and numerical methods used are presented, followed by discussions on the results and the conclusions drawn from this study.

2. Governing equations

The governing equations for the gas–liquid two-phase flow are based on the conservation laws. The injected liquid is taken as incompressible with the surrounding gas fully compressible and treated as an ideal gas. The flow field is described by the time-dependent Navier–Stokes equations. An idealised axisymmetric flow configuration has been considered, where a thin liquid sheet is located inside an annular gas jet. In this work, the non-dimensional form of the governing equations is employed. The physical space is spanned by a cylindrical coordinate system (x, r, θ), where x is the streamwise direction. The flow is considered to be uniform in the azimuthal direction, i.e. $u_\theta = 0$. Reference quantities used in the normalisation are the maximum streamwise velocity at the jet nozzle exit (domain inlet), the radius of the annular jet (measured from the middle of the annular sheet to the geometrical centre of the axisymmetric domain), the ambient temperature, the ambient gas density and viscosity and the liquid surface tension (assumed to be constant, which results in a non-dimensional value of one). The non-dimensional quantities in the governing equations are: x, streamwise direction; r, radial direction; u, streamwise velocity; v, radial velocity; t, time; γ, ratio of specific heats of the compressible gas; ρ, gas–liquid mixture density; ρ_G, gas density; ρ_L, liquid density (assumed constant); μ, gas–liquid mixture viscosity; μ_G, gas viscosity; μ_L, liquid viscosity (assumed constant); p, gas pressure; T, temperature; Y, liquid mass fraction; Φ, liquid volume fraction; κ, curvature; σ, surface tension; $E_T = \rho_G\,[e + (u^2 + v^2)/2]$, total energy of the gas with e representing the internal energy per unit mass; Ma, Mach number; Pr, Prandtl number; Re, Reynolds number; Sc, Schmidt number; and We, Weber number.

The governing equations are formulated upon the conservation laws for mass, momentum and energy and they

describe both phases in a single set of equations. In the Eulerian approach with mixed-fluid treatment adopted (Crowe, 2006), there is no distinction between the velocities of the two phases, while the density and viscosity are considered as gas–liquid mixture properties. In the current formulation a non-reacting isothermal flow is considered, where the two phases exchange only momentum without phase change and energy transfer taking place. The continuity equation for the gas phase is given by

$$\frac{\partial \rho_G}{\partial t} = -\frac{\partial(\rho_G u)}{\partial x} - \frac{1}{r}\frac{\partial(\rho_G v r)}{\partial r}. \tag{1}$$

The Navier–Stokes momentum equations for the gas–liquid two-phase flow take into account the effect of surface tension and are given by the following two equations

$$\frac{\partial(\rho u)}{\partial t} = -\frac{\partial(\rho u^2 + p - \tau_{xx})}{\partial x} - \frac{1}{r}\frac{\partial[(\rho uv - \tau_{xr})r]}{\partial r} + \frac{\sigma\kappa}{We}\frac{\partial \Phi}{\partial x}, \tag{2}$$

$$\frac{\partial(\rho v)}{\partial t} = -\frac{\partial(\rho uv - \tau_{xr})}{\partial x} - \frac{1}{r}\frac{\partial[(\rho v^2 + p - \tau_{rr})r]}{\partial r} - \frac{-p + \tau_{\theta\theta}}{r} + \frac{\sigma\kappa}{We}\frac{\partial \Phi}{\partial r}, \tag{3}$$

where the constitutive relations for viscous stress components τ_{xx}, τ_{xr}, τ_{rr} and $\tau_{\theta\theta}$ are given in Table 1. For the isothermal flow considered, neglecting the effects of liquid on the gas temperature, the energy equation for the gas phase is given by

$$\frac{\partial E_T}{\partial t} = -\frac{\partial[(E_T + p)u + q_x - u\tau_{xx,G} - v\tau_{xr,G}]}{\partial x} - \frac{1}{r} \times \frac{\partial\{[(E_T + p)v + q_r - u\tau_{xr,G} - v\tau_{rr,G}]r\}}{\partial r}, \tag{4}$$

where the gas-phase heat flux components q_x, q_r, and the viscous stress components $\tau_{xx,G}$, $\tau_{xr,G}$, $\tau_{rr,G}$ are given in Table 1. To allow for the gas compressibility to be considered, the transport equation for liquid mass fraction is utilised, rather than the transport equation for liquid volume fraction which is applicable to incompressible flows only. The transport equation for the liquid concentration per unit volume ρY, including the effect of mass diffusion, can be given as

Table 1
The constitutive relations for viscous stress and heat flux components

Gas–liquid mixture	Gas
$\tau_{xx} = -\frac{2}{3}\frac{\mu}{Re}\left(-2\frac{\partial u}{\partial x} + \frac{\partial v}{\partial r} + \frac{v}{r}\right)$	$\tau_{xx,G} = -\frac{2}{3}\frac{\mu_G}{Re}\left(-2\frac{\partial u}{\partial x} + \frac{\partial v}{\partial r} + \frac{v}{r}\right)$
$\tau_{xr} = \frac{\mu}{Re}\left(\frac{\partial v}{\partial x} + \frac{\partial u}{\partial r}\right)$	$\tau_{xr,G} = \frac{\mu_G}{Re}\left(\frac{\partial v}{\partial x} + \frac{\partial u}{\partial r}\right)$
$\tau_{rr} = -\frac{2}{3}\frac{\mu}{Re}\left(\frac{\partial u}{\partial x} - 2\frac{\partial v}{\partial r} + \frac{v}{r}\right)$	$\tau_{rr,G} = -\frac{2}{3}\frac{\mu_G}{Re}\left(\frac{\partial u}{\partial x} - 2\frac{\partial v}{\partial r} + \frac{v}{r}\right)$
$\tau_{\theta\theta} = -\frac{2}{3}\frac{\mu}{Re}\left(\frac{\partial u}{\partial x} + \frac{\partial v}{\partial r} - 2\frac{v}{r}\right)$	$q_x = \frac{-\mu_G}{(\gamma-1)Ma^2 PrRe}\frac{\partial T}{\partial x}$
	$q_r = \frac{-\mu_G}{(\gamma-1)Ma^2 PrRe}\frac{\partial T}{\partial r}$

$$\frac{\partial(\rho Y)}{\partial t} = -\frac{\partial(\rho u Y)}{\partial x} - \frac{1}{r}\frac{\partial[(\rho v Y)r]}{\partial r} + \frac{1}{ReSc}\frac{\partial}{\partial x}\left(\mu\frac{\partial Y}{\partial x}\right) + \frac{1}{ReSc}\frac{1}{r}\frac{\partial}{\partial r}\left[\left(\mu\frac{\partial Y}{\partial r}\right)r\right]. \tag{5}$$

Assuming the gas medium as ideal gas, the governing equations for the gas–liquid two-phase flow system include also the perfect gas law, given by

$$p = \frac{\rho_G T}{\gamma Ma^2}. \tag{6}$$

The physics of the gas–liquid interface are computed and analysed using the volume of fluid (VOF) method by Hirt and Nichols (1979), which employs the liquid volume fraction. The liquid volume fraction works as an indicator to identify the different fluids. A liquid volume fraction value of one, $\Phi = 1$, corresponds to pure liquid and a value of zero, $\Phi = 0$, corresponds to pure gas. In between the two values, $0 < \Phi < 1$, a gas–liquid interface region exists and the fluid is considered as a mixture. In this study, the original VOF method has been adapted to solve an equation for the liquid mass fraction Y rather than the volume fraction Φ in order to suit the compressible gas phase formulation. From their definitions, a relation between liquid volume fraction and mass fraction can be derived as

$$\Phi = \frac{\rho_G Y}{\rho_L - (\rho_L - \rho_G)Y}. \tag{7}$$

Following De Villiers et al. (2004), the density and viscosity of the gas–liquid two-phase fluid flow are considered as functions of the liquid volume fraction and densities and viscosities of both phases, given by

$$\rho = \Phi\rho_L + (1 - \Phi)\rho_G, \tag{8}$$

$$\mu = \Phi\mu_L + (1 - \Phi)\mu_G. \tag{9}$$

Eqs. (8) and (9) are utilised in conjunction with the VOF method, to account for the contributions of the two individual phases to the mixture properties (De Villiers et al., 2004; Gao et al., 2003; Gueyffier et al., 1999). The linear relation between the properties of the mixture and the individual phases is required by the Eulerian approach with mixed-fluid treatment for the multi-phase flow (Crowe, 2006), which ensures that the two phases both satisfy the Navier–Stokes equations. The gas–liquid interface dynamics are resolved using a continuum surface force (CSF) model developed by Brackbill et al. (1992), which represents the surface tension effect as a continuous volumetric force acting within the region where the two phases coexist. The CSF model overcomes the problem of directly computing the surface tension integral that appears in the Navier–Stokes momentum equations, which requires the exact shape and location of the interface.

In the CSF model, the surface tension force in its non-dimensional form, as it appears in Eqs. (2) and (3), can be approximated as $\sigma\kappa/We\nabla\Phi$, with the curvature of the interface given by

$$\kappa = -\nabla\cdot\left(\frac{\nabla\Phi}{|\nabla\Phi|}\right) = -\frac{\partial}{\partial x}\left\{\frac{\partial\Phi}{\partial x}\left[\left(\frac{\partial\Phi}{\partial x}\right)^2+\left(\frac{\partial\Phi}{\partial r}\right)^2\right]^{-\frac{1}{2}}\right\} - \frac{\partial}{\partial r}\left\{\frac{\partial\Phi}{\partial r}\left[\left(\frac{\partial\Phi}{\partial x}\right)^2+\left(\frac{\partial\Phi}{\partial r}\right)^2\right]^{-\frac{1}{2}} r\right\}. \quad (10)$$

The governing equations at the domain centreline have been put into a special form to avoid the singularities in the mathematical formulation (Jiang and Luo, 2000; Jiang et al., 2004a,b) and they were derived from the original equations using l'Hôspital's rule. This enables precise definition of the symmetry conditions. The new set of governing equations at the domain centreline is given by

$$\frac{\partial\rho_G}{\partial t} = -\frac{\partial(\rho_G u)}{\partial x} - 2\frac{\partial(\rho_G v)}{\partial r}, \quad (11)$$

$$\frac{\partial(\rho u)}{\partial t} = -\frac{\partial(\rho u^2+p-\tau_{xx})}{\partial x} - 2\frac{\partial(\rho uv-\tau_{xr})}{\partial r} + \frac{\sigma\kappa}{We}\frac{\partial\Phi}{\partial x}, \quad (12)$$

$$\frac{\partial(\rho v)}{\partial t} = -\frac{\partial(\rho uv-\tau_{xr})}{\partial x} - \frac{\partial(\rho v^2+p-\tau_{rr})}{\partial r} - \frac{\partial(\rho v^2-\tau_{rr}+\tau_{\theta\theta})}{\partial r} + \frac{\sigma\kappa}{We}\frac{\partial\Phi}{\partial r}, \quad (13)$$

$$\frac{\partial E_T}{\partial t} = -\frac{\partial[(E_T+p)u+q_x-u\tau_{xx,G}-v\tau_{xr,G}]}{\partial x} - 2\frac{\partial[(E_T+p)v+q_r-u\tau_{xr,G}-v\tau_{rr,G}]}{\partial r}, \quad (14)$$

$$\frac{\partial(\rho Y)}{\partial t} = -\frac{\partial(\rho uY)}{\partial x} - 2\frac{\partial(\rho vY)}{\partial r} + \frac{1}{ReSc}\frac{\partial}{\partial x}\left(\mu\frac{\partial Y}{\partial x}\right) + 2\frac{1}{ReSc}\frac{\partial}{\partial r}\left(\mu\frac{\partial Y}{\partial r}\right). \quad (15)$$

The centreline singularity of the curvature relation in Eq. (10) and the centreline singularities of the constitutive relations for viscous stress components in Table 1 can also be avoided by applying l'Hôspital's rule.

3. Numerical methods

The numerical methods include the high-order finite-difference schemes for time advancement and spatial discretisation. The governing equations are integrated forward in time using a third-order compact-storage fully explicit Runge–Kutta scheme (Williamson, 1980). The solution variables (ρ_G, ρu, ρv, E_T, ρY) in Eqs. (1)–(5) and (11)–(15) are advanced in time using a three-step compact-storage third-order Runge–Kutta scheme of the family derived by Wray (1986). Two storage locations are employed for each time-dependent variable and at each sub-step at these locations, say Q_1 and Q_2 with Q representing the solution variables, are updated simultaneously as follows

$$Q_1^{new} = a_1\Delta t Q_1^{old} + Q_2^{old}, \quad Q_2^{new} = a_2\Delta t Q_1^{old} + Q_2^{old}. \quad (16)$$

The constants (a_1, a_2) in Eq. (16) are chosen to be $(2/3, 1/4)$ for sub-step 1, $(5/12, 3/20)$ for sub-step 2 and $(3/5, 3/5)$ for sub-step 3. At the beginning of each full time step, Q_1 and Q_2 are equal. The data in Q_1 is used to compute the right hand side of Eqs. (1)–(5) and (11)–(15). The computed right hand side is stored in Q_1 (overwriting the old Q_1). Eq. (16) is then used to update Q_1 and Q_2. In Eq. (16), Δt is the time step, which is limited by the Courant–Friedrichs–Lewy (CFL) condition for stability.

During the time advancement, the density and viscosity of the gas–liquid two-phase flow system are calculated according to Eqs. (8) and (9), using the volume fraction Φ calculated from Eq. (7). However, the liquid mass fraction Y in Eq. (7) needs to be calculated from the solution variable ρY first. Using q_5 to represent ρY at each time step, the liquid mass fraction Y can be calculated as

$$Y = \frac{\rho_L q_5}{\rho_L\rho_G + (\rho_L-\rho_G)q_5}. \quad (17)$$

Eq. (17) can be derived from Eqs. (7) and (8). At each time step, Eq. (17) is used first to calculate the liquid mass fraction, Eq. (7) is then used to calculate the liquid volume fraction and Eqs. (8) and (9) are finally used to update the mixture density and viscosity.

Spatial differentiation is achieved by using the high-order compact (Padé) finite-difference scheme of Lele (1992), which is of sixth-order at inner points, of fourth order at the next to the boundary points and of third-order at the boundary, thus it has been called the Padé 3/4/6 scheme. For a variable ϕ_j at grid point j in the cross-streamwise direction, the sixth order Padé scheme at the inner points can be written in the following form for the first and second derivatives

$$\phi'_{j-1} + 3\phi'_j + \phi'_{j+1} = \frac{7}{3}\frac{\phi_{j+1}-\phi_{j-1}}{\Delta\eta} + \frac{1}{12}\frac{\phi_{j+2}-\phi_{j-2}}{\Delta\eta}, \quad (18)$$

$$\phi''_{j-1} + \frac{11}{2}\phi''_j + \phi''_{j+1} = 6\frac{\phi_{j+1}-2\phi_j+\phi_{j-1}}{\Delta\eta^2} + \frac{3}{8}\frac{\phi_{j+2}-2\phi_j+\phi_{j-2}}{\Delta\eta^2}, \quad (19)$$

where $\Delta\eta$ is the mapped grid distance in the radial direction, which is uniform in space (grid mapping occurs when non-uniform grid is used). By applying the symmetry conditions to both the primitive variables and their first and second derivatives in the radial direction, the Padé 3/4/6 scheme has been extended to achieve the formal sixth-order accuracy at the domain centreline (Jiang and Luo, 2000), which is a boundary of the computational domain.

The discretisation of Eqs. (1)–(5) and (11)–(15) forms a set of discretised equations whose solutions are obtained by solving the tridiagonal system of equations. The interface curvature in Eq. (10) is a function of the derivatives of the liquid volume fraction and is also discretised according to the Padé 3/4/6 scheme.

The grid system used is of the form used by Luo and Sandham (1997), which is uniformly distributed in the

x-direction and stretched in the r-direction. The mapped grid in the radial direction uses a hyperbolic sine function and concentrates points around the centre of the thin liquid sheet inside the annular gas jet. The mapped grid in the radial direction is utilised to resolve more efficiently the flow fields near the liquid sheet, the surface tension and the gas-phase vortical structures.

The boundary conditions in the DNS performed are difficult to treat because the sixth-order finite difference scheme has no dissipation and very low dispersion errors. This results in the need for an appropriate and precise specification of the boundary conditions to avoid numerical instabilities and to control the spurious wave reflections at the computational boundaries. At the same time the boundary conditions must be able to represent the physical conditions at the boundaries as realistically as possible. There are four boundaries for the computational domain which represents a half cross-section of the axisymmetric domain: (1) the symmetry boundary at the geometrical centre of the annular jet $r = 0$; (2) the far side boundary in the radial direction $r = L_r$; (3) an inflow boundary at the domain inlet (jet nozzle exit) $x = 0$; and (4) an outflow boundary downstream the computational box $x = L_x$.

At the inflow boundary, the Navier–Stokes characteristic boundary condition (NSCBC) of Poinsot and Lele (1992) is used. The NSCBC is compatible with the sixth-order non-dissipative algorithms used for the spatial DNS. It uses also the correct number of boundary conditions required for well-posedness of the Navier–Stokes equations that can avoid numerical instabilities and spurious wave reflections at the computational boundaries. A "soft" boundary is used for the equation of total energy, meaning that the temperature is left free to ensure numerical stability while other variables are imposed at the inflow boundary. In the numerical simulations the variation of temperature at the inflow is negligible. A hyperbolic tangent profile (Jiang et al., 2004a) has been used for the streamwise velocity. At the domain inlet the radial velocity is taken as zero. The mass fraction of the thin liquid sheet located around $r_0 = 1$ is also assumed to have a "top-hat" profile, given by

$$Y = \frac{1}{2}\left\{1 - \tanh\left[\frac{R_L}{4\delta_2}\left(\frac{|r - r_0|}{R_L} - \frac{R_L}{|r - r_0|}\right)\right]\right\}. \quad (20)$$

This profile is similar to the velocity profile where the initial momentum thickness (Michalke, 1984) is specified as $\delta_2 = 0.1$, which has also been used in the specification of mass fraction in Eq. (20). The thickness of the liquid sheet R_L in Eq. (20) is given in Table 2 for the six computational cases.

At the outflow boundary in the streamwise direction, the nonreflecting characteristic boundary conditions due to Thompson (1987) are applied. A sponge layer next to the outflow boundary is also used to control the spurious wave reflections from the outside of the computational domain (Jiang and Luo, 2000). The strategy of using a sponge layer is similar to that of "sponge region" or "exit zone" (Mitchell et al., 1999), which has been proved to be very effective in controlling the wave reflections through the outflow boundary. The results of the sponge layer are unphysical and therefore are not used in the data analysis as they do not affect the results at upstream locations.

Table 2
The computational cases

	Case A	Case B	Case C	Case D	Case E	Case F
Weber number, We	240	240	480	∞	240	240
Liquid sheet thickness, R_L	0.01	0.02	0.02	0.02	0.01	0.01
Density ratio, (ρ_L/ρ_G)	5	5	5	5	2.5	5
Viscosity ratio, (μ_L/μ_G)	24	24	24	24	24	12

Nonreflecting characteristic boundary conditions due to Thompson (1987) are used at the far side boundary in the radial direction $r = L_r$, which prevent the wave reflections from the outside of the computational domain and allow entrainment of the ambient fluids. For the symmetry boundary at the geometric centre of the annular configuration, symmetry conditions are applied and there is no need to apply any additional boundary conditions based on the analysis of characteristics since there is no fluid penetrating the symmetry line in the idealised axisymmetric configuration.

4. Results and discussion

4.1. Simulation details

Simulations have been performed to examine the effects of liquid sheet thickness, surface tension, and liquid-to-gas density and viscosity ratios on flow characteristics of the gas–liquid two-phase flow. Numerical results from the six computational cases shown in Table 2 will be presented and discussed. In all the cases performed, the width of the annular jet is 0.2 with a thin liquid sheet (thickness given in Table 2) located in the middle of the compressible gas. In Table 2, the parameters used for Cases A and B correspond to diesel injection into compressed air at approximately 15 MPa and 300 K, where the liquid surface tension is around 0.025 N/m and takes a unit non-dimensional value based on the reference quantities mentioned in Section 2. The input parameters used in the simulations for all the computational cases are: jet Mach number $Ma = 0.4$; Reynolds number $Re = 2000$; Prandtl number $Pr = 0.76$; Schmidt number $Sc = 0.76$ and ratio of specific heats $\gamma = 1.64$. These parameters were estimated from values given by Perry and Green (1998). In Table 2, the liquid sheet thickness of Case B is doubled from its value in Case A to examine its effect. Cases B, C and D have been performed to examine the effect of liquid surface tension. In Case D, the surface tension has been switched off to isolate its effect. An infinite Weber number represents a case without surface tension. In Case C, the Weber number was doubled from its value in Case B. In Table 2, Cases E and F have been performed to examine the effects of

liquid-to-gas density and viscosity ratios respectively, where the comparison between Cases A and E can be used to elucidate the effect of density ratio while the comparison between Cases A and F can be used to elucidate the effect of viscosity ratio.

The numerical methods used in the code have been previously well-tested and validated for different applications of single-phase gas jets (Jiang and Luo, 2000; Jiang et al., 2004a,b). In this study, the dimensions of the computational box $[0 \sim L_x,\ 0 \sim L_r]$ are $L_x = 20r_0$ with $L_{xs} = 18r_0$, and $L_r = 10r_0$, where $L_{xs} < x \leqslant L_x$ is the sponge layer. The grid system used is of 1351×600 nodes. The grid has a uniform distribution in the streamwise direction, while it is stretched in the radial direction to include a sufficient number of points around the annular jet. In this study, a grid independence test has been performed, following the grid refinement study performed previously to determine the optimum grid (Jiang and Luo, 2000). A CFL number of 2.0 is used, which has been tested to give time-step independent results. A domain size test has also been performed to guarantee the results are independent of the domain size in the radial direction (Jiang and Luo, 2000). The results presented next are therefore considered to be grid, time-step and domain-size independent and accurate in terms of the physical conditions specified. The results will be presented for both instantaneous and time-averaged flow properties and discussed in terms of the effects of liquid sheet thickness, liquid surface tension, and liquid-to-gas density and viscosity ratios on the flow structures, velocity histories and liquid topology. For clarity, the results in the contour and vector plots are shown for a part, but for both sides, of the axisymmetric domain used for the simulation of the annular jet. In most of the figures shown below, subtitles a, b, c, d, e and f represent for Cases A, B, C, D, E and F, respectively.

4.2. Instantaneous liquid topology and flow characteristics

Fig. 1 shows the instantaneous liquid volume fraction contours at $t = 100$ for the six computational cases. It is clear that in all cases the annular jet exhibits formation of a "bell shape" near the nozzle exit plane, as described by Ibrahim and McKinney (2006). This is because upon emerging from the nozzle exit the jet has the tendency to

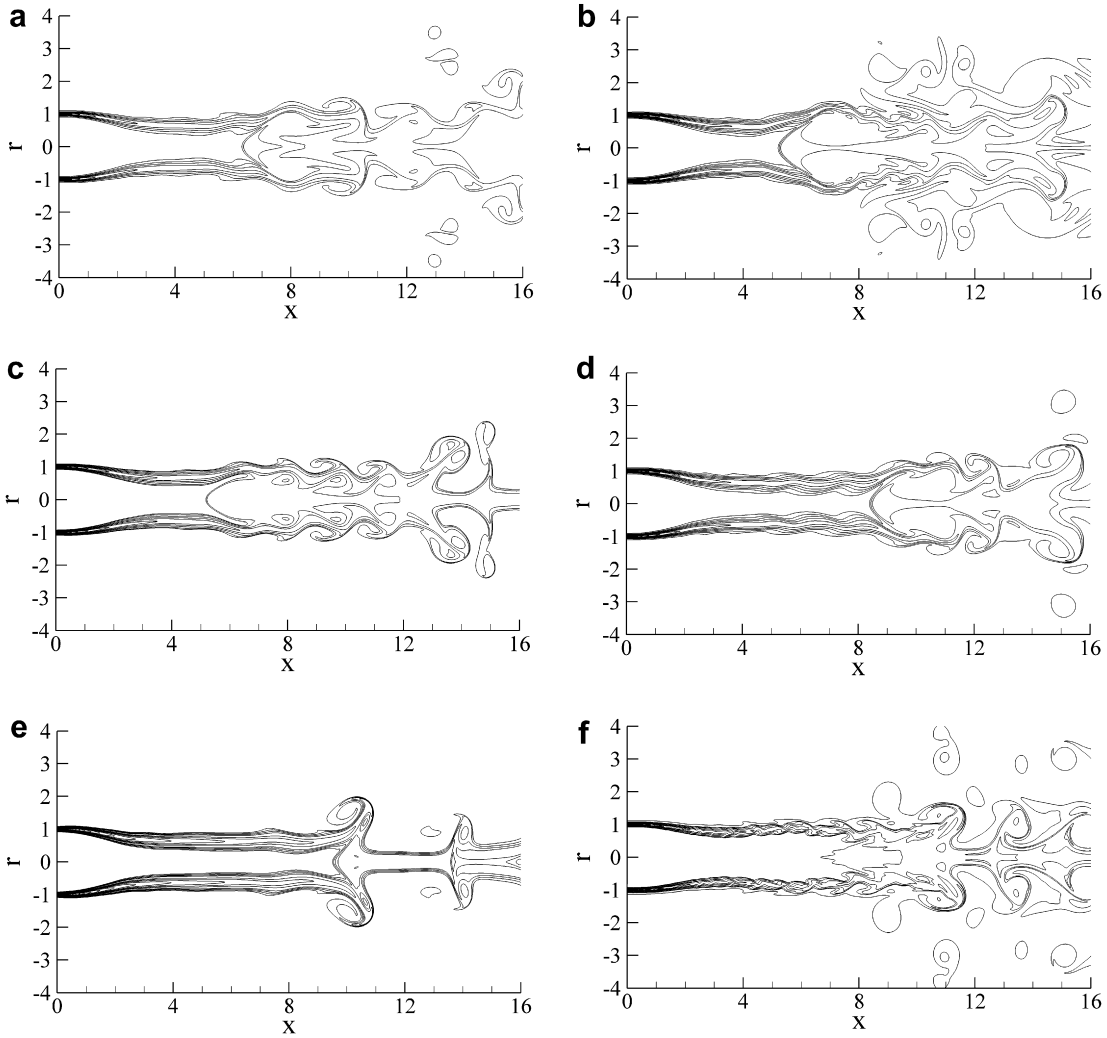

Fig. 1. Instantaneous liquid volume fraction contours at $t = 100$.

continuously converge towards the centreline. The annular jet collapses further downstream the computational domain and it spreads in the cross-streamwise direction when the collapse is taking place. There is also a tendency of liquid breakup. In Fig. 1, it is evident that a shorter "bell shape" corresponds to a larger downstream spreading, which is expected as they both correspond to a stronger mixing of the annular jet with its ambient environment. By comparing Cases A and B, shown in Figs. 1a and b, it is evident that in Case A the jet exhibits a more elongated "bell shape". The "bell shape" in Case A collapses at around $x = 6.5$, while it collapses at $x = 5.5$ in Case B. Case B has also a much larger spreading at the further downstream locations. An increase in sheet thickness leads to a faster flow development of the annular jet, resulting in faster converging towards the centreline and larger downstream spreading. This trend is in good agreement with the findings of Lin (2003) regarding the manifestation of the destabilizing effect of interfacial shear.

For the effect of surface tension on the flow development, comparing Figs. 1b–d, it can be seen that surface tension promotes flow instability which in turn enhances the mixing of the annular jet with its ambient environment. This agrees with findings from linear stability analysis of surface tension effect on axisymmetric and annular jets (Sirignano and Mehring, 2000; Shen and Li, 1995; Lin, 2003). It is evident that in Case C, where the surface tension effect is accounted for, the jet tends to spread more than in Case D. Further increase of the surface tension tends to spread the jet even more as shown by comparing Cases B and C. A decreased elongation of the "bell shape" is noticed when surface tension is included in the simulation. In the annular gas–liquid two-phase flow, where the two phases are not considered to have different local velocities in an Eulerian approach with mixed-fluid treatment, surface tension promotes flow instability and thus increases the cross-streamwise dispersion of the liquid jet. The importance of surface tension in the instability promotion was also noticed by Cao (2003).

The effect of density ratio on the flow development is clear by comparing Fig. 1a and e. Case A is more vortical than Case E since the increased liquid-to-gas density ratio amplifies the instability. This trend is consistent with the observations of Lin (2003), Shen and Li (1995) and Rangel and Sirignano (1988). It is worth noticing that the trend is opposite to that found by Shen and Li (1996) who assumed the jet to be inviscid. The increased liquid-to-gas density ratio tends to gradually increase the cross-streamwise dispersion of the liquid.

Cases A and F show the effects of the liquid-to-gas viscosity ratio on the flow field. It is evident that Case F is more vortical than Case A. The decreased viscosity ratio in Case F tends to promote the instability since reduced viscosity tends to destabilize the flow field. This observation is consistent with the findings of Lin (2003). In Case F, vortical structures started their formations very close to the jet nozzle exit in the upstream locations of the annular column. The cross-streamwise dispersion of the liquid in Case F is increased, as expected. It is interesting to see that density and viscosity ratios have opposite effects on the flow development since a decreased density ratio stabilizes the flow while a decreased viscosity ratio has destabilizing effects.

The instantaneous velocity vector plots at $t = 100$ for the six cases are shown in Fig. 2. For clarity the vectors are plotted for a limited number of points which is significantly fewer than the total number of grid points. At $t = 100$, the flow can be considered as fully developed since the jet has passed through the computational domain several times. It can be seen that the flow has developed a variety of vortical structures. The most noticeable feature in Fig. 2 is that the flow has two significant velocity reversals along the centreline. In all cases, the first velocity reversal occurs very close to the jet nozzle exit plane, which is due to the formation of a recirculation zone adjacent to the nozzle exit before $x = 3$. This formation of a recirculation zone close to the nozzle exit is a common feature of annular jet flow as it was also experimentally observed by Del Taglia et al. (2004) and Sheen et al. (1996). In Fig. 2, an important observation is that the second velocity reversal, which occurs at downstream locations along the centreline, corresponds exactly to the locations where the collapse of the annular jet takes place. In Cases A, B, C and D, the second velocity reversal occurs approximately at $x = 6.5$, $x = 5.5$, $x = 5.0$ and $x = 8.5$, respectively. Case E shows no formation of a second velocity reversal zone mainly due to the stable flow field associated with the reduced density ratio. The increased instability found in Case F caused the second velocity reversal zone to be adjacent to the recirculation zone as shown in Fig. 2f. The second velocity reversal is mainly owed to the formation of large-scale vortical structures at the downstream locations. It is interesting to notice that in all cases the recirculation zones adjacent to the jet nozzle exit have similar locations, while the downstream vortical structures are quite different. In order to clearly represent the vortical structures in the flow field, the instantaneous vorticity contours are shown next.

Fig. 3 shows the instantaneous vorticity distributions at $t = 100$. In the axisymmetric annular simulations performed herein only the azimuthal vorticity $\omega_\theta = \partial v/\partial x - \partial u/\partial r$ is shown since it is the only vorticity component which is nonzero. Both negative and positive vorticity are present, which is due to the fact that the liquid sheet has two adjacent shear layers with opposite sign velocity gradients. In Fig. 3 the formation of vortical structures at the downstream locations is evident. The formation of vortical structures is mainly associated with the development of the Kelvin–Helmholtz instability, which occurs when velocity shear is present within a continuous fluid or when there is sufficient velocity difference across the interface between two fluids. In the mixed-fluid treatment adopted in this study, there is no velocity difference across the interface between the two fluids and thus the development of the Kelvin–Helmholtz instability is due to the presence of the two velocity shear layers located at around $r = 1$.

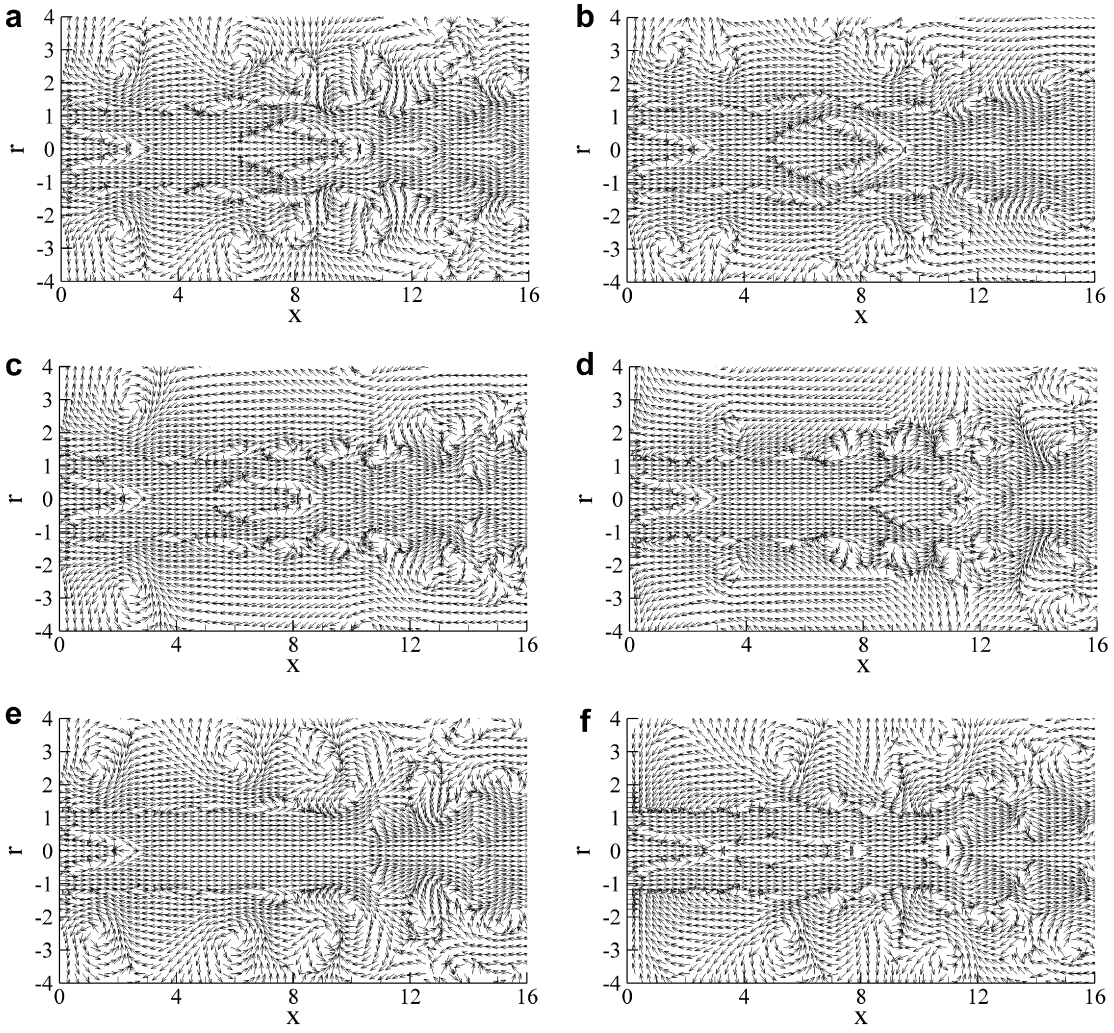

Fig. 2. Instantaneous velocity vector plots at $t = 100$.

For liquid breakup and atomisation modelling, the Kelvin–Helmholtz instability is one of the major instabilities considered (Stiesch, 2003). A noticeable aspect in the simulations performed is that no external perturbation was applied at the inflow to trigger the Kelvin–Helmholtz instability, unlike the simulations of axisymmetric jets (Jiang et al., 2004a) where an external perturbation was essential to initiate the Kelvin–Helmholtz instability. In this study, the annular jet flow showed naturally developed flow instabilities, where the development of vortical structures does not depend on the continuous supply of external perturbations. Such instability might be triggered by the mismatch between the initial conditions specified and the exact solution of the Navier–Stokes equations. The growth of the flow instability leads to the formation of large-scale vortical structures in the flow field, which subsequently control the mixing of the fluids and dominate the flow characteristics.

To further examine the velocity reversals at the jet centreline, Fig. 4 shows the instantaneous centreline velocity profiles at $t = 100$ for all the cases under investigation. The characteristic feature in Fig. 4 is that in all cases, apart from Case F, the centreline velocity drops from the zero value at the inlet to a value of approximately -0.6 at the location $x = 0.5$, which then gradually increases to a value of zero at approximately $x = 3.0$. This velocity behaviour is due to the recirculation zone adjacent to the nozzle exit. Further downstream negative values of velocity appear again, because of the second velocity reversal associated with the formation of a large-scale vortical structure as shown in Fig. 2. The velocity variations at the jet centreline are due to the large-scale vortical structures developed in the flow field. In Case F the dropped centreline velocity continues to have negative values up to the location of $x = 8.0$ due to the velocity reversals associated with the vortical structure adjacent to the recirculation zone. For all the cases in Fig. 4, Case B shows the largest velocity variations due to the strong mixing associated with the vortical structures in this case. The increased liquid sheet thickness tends to increase the velocity variations at the centreline, as it can be seen by comparing Cases A and B. By comparing Cases B, C and D it is clear that surface tension promotes vorticity. Case E does not show any negative velocity, apart from the recirculation zone adjacent to the nozzle exit, due to the non-existence of a second veloc-

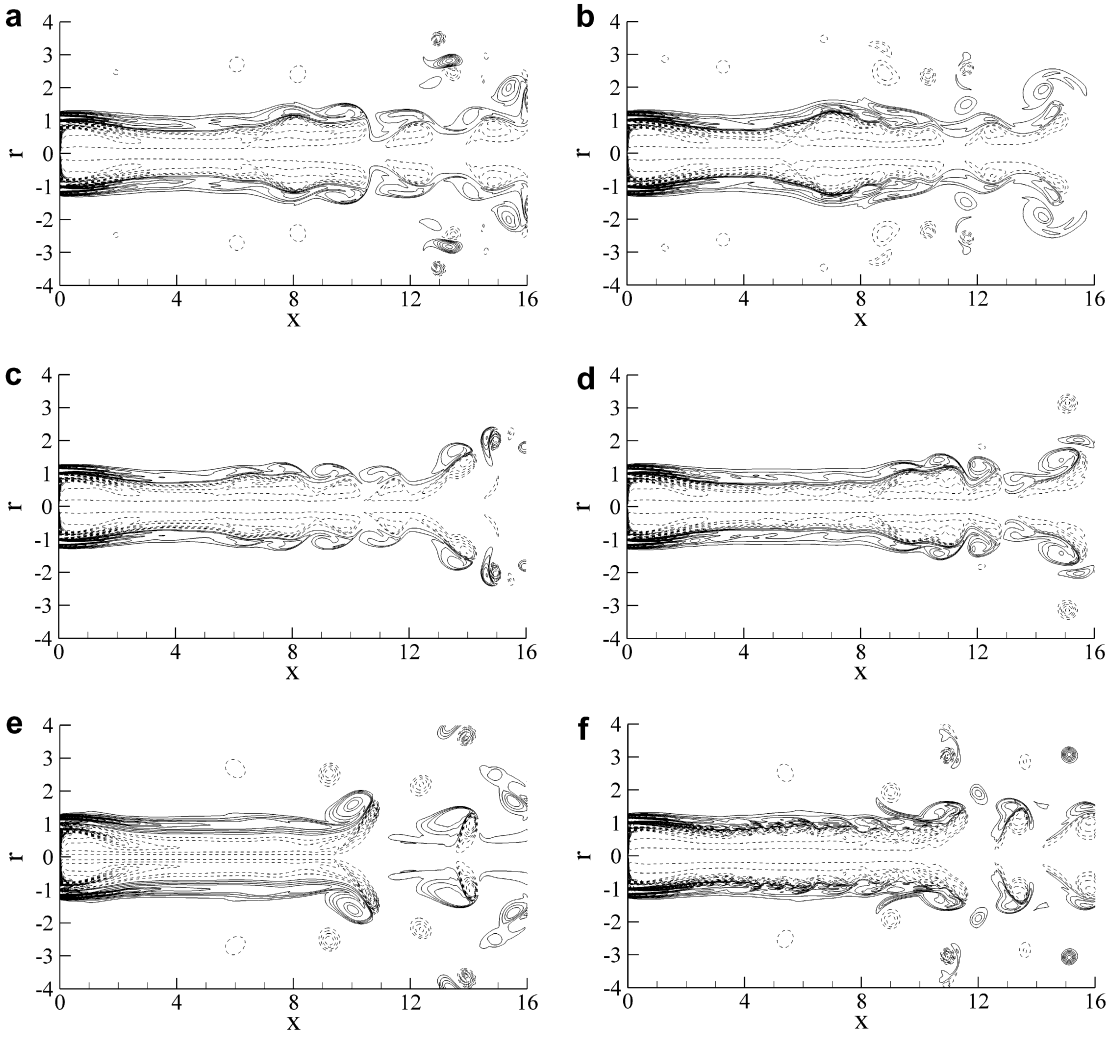

Fig. 3. Instantaneous vorticity contours at $t = 100$ (solid line: positive; dashed line: negative).

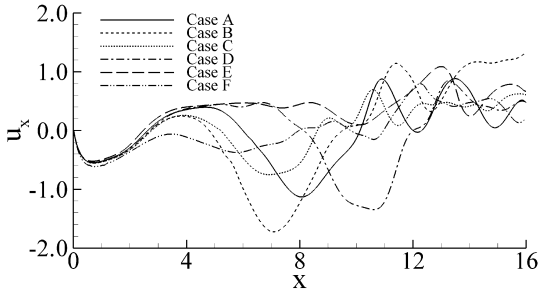

Fig. 4. Instantaneous centreline velocity profiles at $t = 100$.

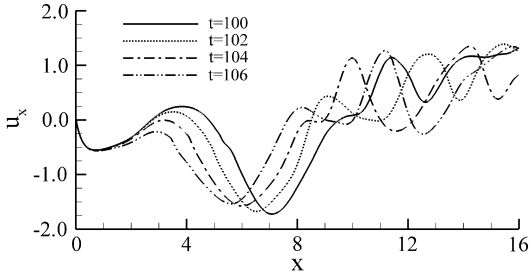

Fig. 5. Instantaneous centreline velocity profiles of Case B at different time instants.

ity reversal zone in the flow field. The stable flow field in Case E does not enable development of large-scale vortical structures. From Cases E and F it is clear that the liquid-to-gas density and viscosity ratios have opposite effects on the flow development with the reduced density ratio having demoting vorticity characteristics and the reduced viscosity ratio having promoting vorticity trends. These observations are consistent with linear theories (Lin, 2003; Shen and Li, 1995).

The instantaneous centreline velocity profiles in Case B at different time instants are shown in Fig. 5. It is clear that the recirculation zone very close to the jet nozzle exit, exhibits a stationary behaviour since the velocity profiles are overlapping each other from $x = 0$ to $x = 2.0$. Further downstream, significant velocity variations are evident indicating the formation of large-scale vortical structure in the flow field which has a dynamic behaviour. From Fig. 5 it is clear that the annular liquid jet shows two

characteristic regions along the centreline, which are: (i) a recirculation zone adjacent to the nozzle exit; and (ii) a large-scale vortical structure with negative velocity at the domain centreline downstream the computational domain. The existence of the recirculation zone adjacent to the nozzle exit is associated with the spatial development of the annular flow, due to the formation of a stagnation region when the annular jet flow meets the centreline of the domain at $r = 0$. The downstream vortical structure is mainly associated with the development of the flow instability.

The instantaneous centreline gas density and pressure profiles at $t = 100$ are presented in Fig. 6. As expected the gas density and pressure profiles have a very similar trend since pressure is directly proportional to density in an isothermal environment. By comparing Figs. 6 with Fig. 4 it can be seen that the centreline density and pressure show a trend roughly opposite to the centreline velocity. The profiles of centreline gas density and pressure indicate also the presence of large-scale vortical structures in the flow field. In Case E, the centreline gas density and pressure undergo small fluctuations due to the stabilizing effect of the reduced density ratio on the Kelvin–Helmholtz instability. In Case F, the centreline gas density and pressure undergo small changes mainly because of the proximity of the recirculation zone and the vortical structure and the small size of the vortical structure near the centreline.

The annular gas–liquid two-phase flow exhibits an intrinsic instability that leads to the formation of vortical structures in the flow field. To further examine the fluid dynamic behaviour of the annular jet, time-traces of the streamwise velocities of the annular jet are shown in Fig. 7 for two centreline locations starting from $x = 5$ and progressing further downstream to $x = 15$. It is worth mentioning that at the inlet the centreline streamwise velocity is zero. The velocity variations at $x = 5$ are relatively small while they are much larger at the downstream location $x = 15$. The increased downstream velocity variations are due to the growth of flow instability and the establishment of large-scale vortical structures.

In Fig. 7, it is clear that an increase in liquid sheet thickness results in an increase in the velocity variations, as it can be observed by comparing Figs. 7a and b. Comparing Cases, B, C and D, it can be seen that Case B exhibits the largest centreline velocity variations, since the flow field in Case B is more vortical than the other two. By comparing

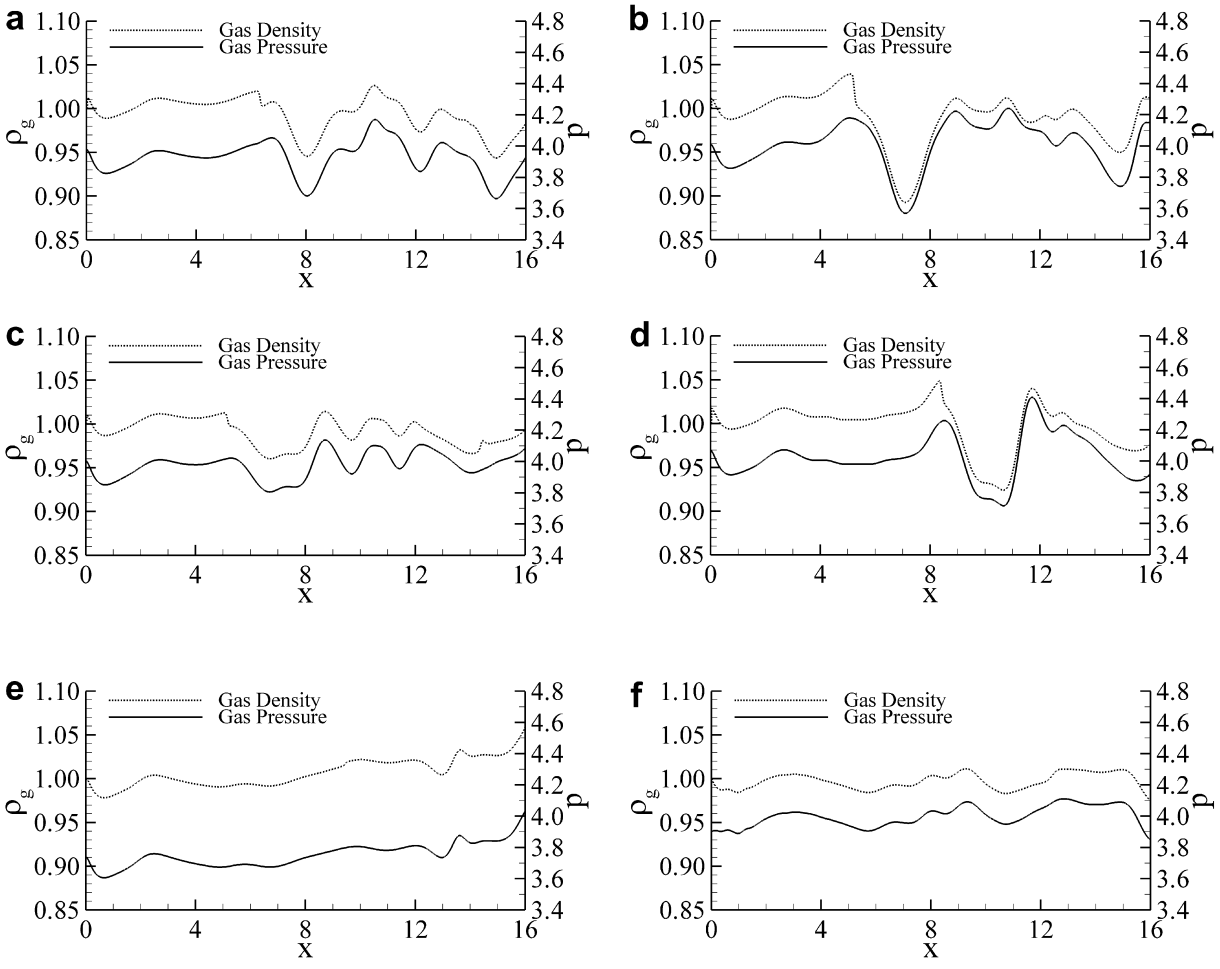

Fig. 6. Instantaneous centreline gas density and pressure profiles at $t = 100$.

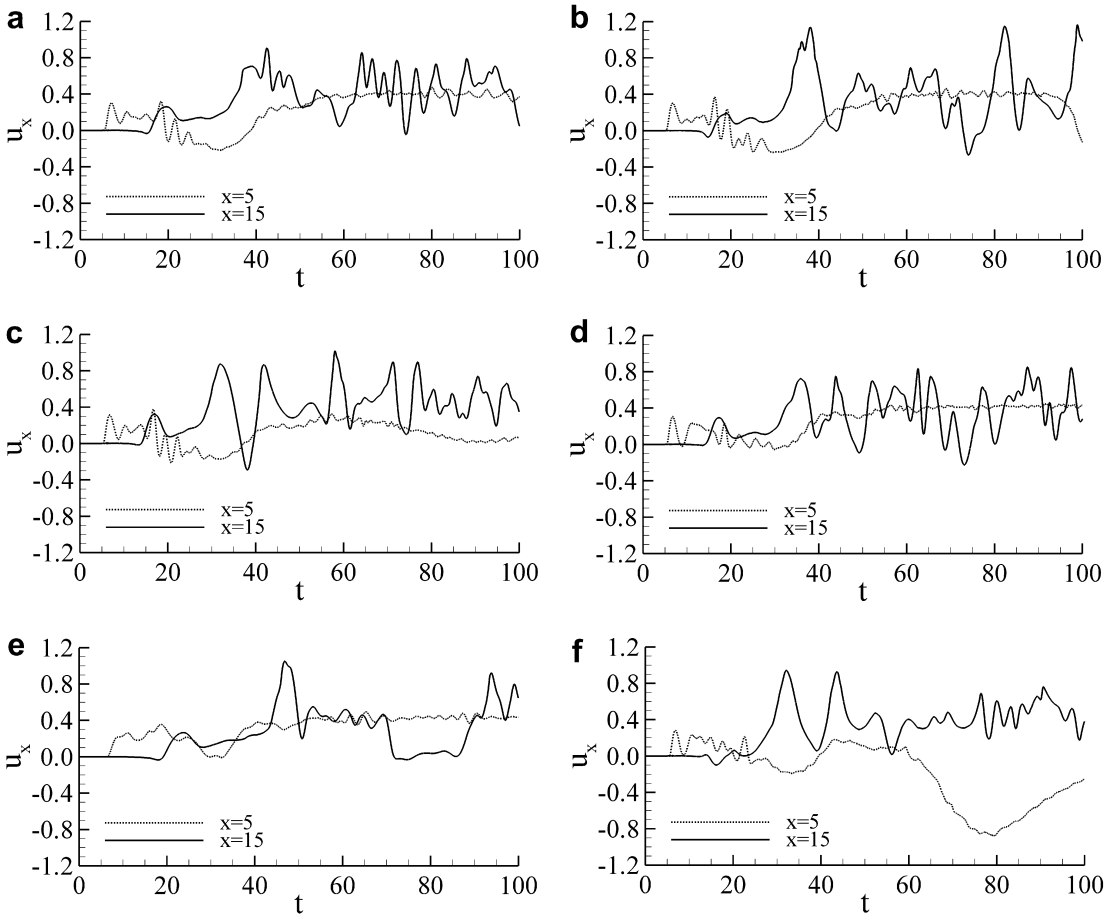

Fig. 7. Centreline streamwise velocity histories at different locations.

Cases A and E it is clear that Case A undergoes more significant velocity fluctuations due to the increased vortical level of the flow field. An opposite trend is observed by comparing Figs. 7a and f since Case F is more unstable than Case A resulting in a more energetic flow field. It is worth noticing that the shape of the centreline velocity profiles at $x = 5$ is similar in all cases apart from Case F. This is primarily owed to the fact that the differences between the computational cases are mainly associated with the development of the vortical structures, which occurs downstream the computational domain. The large velocity variations at $x = 5$, found in Case F, are due to the nature of the second velocity reversal region, which is adjacent to the recirculation zone, that causes formation of large-scale vortical structures at this particular cross-streamwise location.

4.3. Time-averaged flow characteristics

In this study, the time-averaged flow properties have also been calculated to examine the flow characteristics. The time interval used for the calculation of the averaging properties is between $t_1 = 60$ and $t_2 = 100$, after the flow has been fully developed. The large-scale vortical structures at the downstream locations are an instantaneous flow characteristic and they would not be present in the time-averaged results, due to the fact that the vortical structures are continuously convected downstream by the mean flow. In Fig. 8, the time-averaged liquid volume fraction contours are shown.

In Fig. 8, it is evident that in all cases there is a smoothing of the liquid volume fraction due to the time-averaging performed. In all cases the jet exhibits the "bell shape" observed in Fig. 1. Case B shows larger cross-streamwise dispersion compared to Case A, and Cases C and D. This is mainly owed to the effect of the liquid sheet thickness and to the effect of surface tension, both of which affect the flow structure and the dispersion of the liquid in the gas environment. The inclusion of surface tension tends to increase the cross-streamwise dispersion of the liquid while a decreasing liquid sheet thickness tends to oppose the liquid dispersion. The reduced liquid-to-gas density ratio limits the cross-streamwise dispersion of the liquid jet as indicated by comparing Figs. 8a and e, while a reduced liquid-to-gas viscosity ratio tends to increase the liquid dispersion as shown by comparing Cases A and F.

Fig. 9 presents the time-averaged liquid volume fraction profiles at two different locations. It can be noticed that at $x = 5$ the profiles of all cases apart from Case F show a relatively undistorted "top-hat" profile due to the fact that at

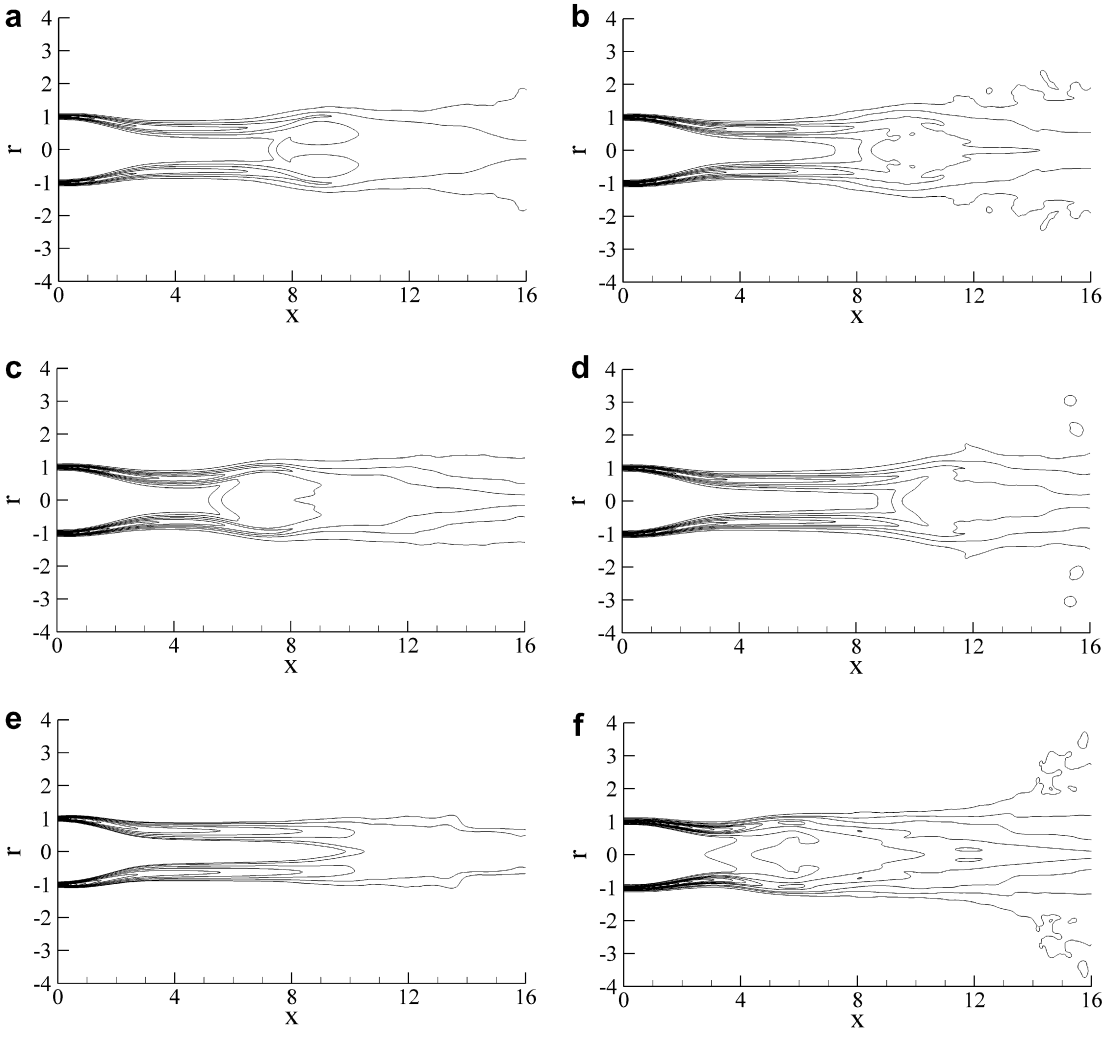

Fig. 8. Time-averaged liquid volume fraction contours.

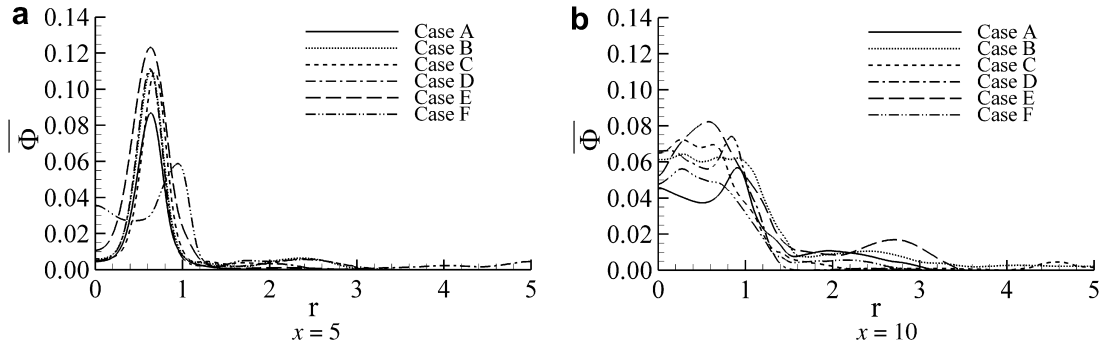

Fig. 9. Time-averaged liquid volume fraction profiles at different cross-streamwise locations.

this location the annular jet has not developed significant flow instabilities and vortical structures. Therefore, the liquid volume fraction is not widely spread and the cases are similar. The slight distortion of the liquid volume fraction profile in Case C is owed to the appearance of the second velocity reversal zone at $x = 5.0$ which disturbs the "top-hat" distribution. This is clearer in Case F where the volume fraction initial profile has fully collapsed since the cross-streamwise position $x = 5.0$ is at the heart of the reversal zone as it was also shown in Fig. 2f. Case E shows the largest liquid volume fraction since the flow field is not as unstable as in the rest of the computational cases. This trend is also noticed at the location $x = 10$. Case A shows a smaller liquid volume fraction due to its reduced liquid sheet thickness, which is quite different from what happens further downstream at $x = 10$. At $x = 10$ the

annular jet shows the largest cross-streamwise dispersion in Cases B and C while it shows the smallest in Case D, as it was also shown in Fig. 1. The volume fraction distribution in Case D is more compact than in Cases B and C since the non-existence of surface tension acts as a stabilizing agent in the development of the Kelvin–Helmholtz instability which affects the dispersion of the liquid. As expected, Case A shows relatively small liquid volume fraction at $x = 10$ due to the thin liquid thickness. Case E shows the largest liquid volume fraction following the trend at $x = 5.0$. The cross-streamwise dispersion in Case F is broader as opposed to Case A as the increased vortical flow field in Case F tends to enlarge the dispersion of the liquid jet.

The time-averaged streamwise velocity contours are shown in Fig. 10. The most important feature in Fig. 10 is the clear capturing of the recirculation zone adjacent to the nozzle exit which is evident from the negative value of the streamwise velocity in this region. The second velocity reversal region next to the domain centreline is captured further downstream, as it was also noticed in Fig. 2, which is due to the collapse of the liquid sheets and further development of the flow vortical structures. In Fig. 10, Cases E and F show different behaviour compared with the other cases. In Case E there is no evidence on the existence of downstream vortical structures, due to the fact that this is the most stable case. An interesting characteristic in Case F is that the second velocity reversal region lies next to the recirculation zone, in agreement with the observation in Fig. 2f.

Fig. 11 shows the time-averaged streamwise velocity profiles at different cross-streamwise locations. It is interesting to see that in all cases, except from Case F, the velocity profiles at $x = 5$ remain similar since the annular liquid sheet has not yet collapsed. In Case F the presence of the second velocity reversal region at $x = 5$ affects the flow velocity as indicated by the large negative velocity value. All cases show decreasing velocity magnitudes at progressive downstream locations, due to the mixing of the annular jet with its ambient environment. At $x = 10$ Case B shows a larger negative velocity magnitude at $r = 0$ indicating a stronger and more energetic large vortical structure next to the domain centreline.

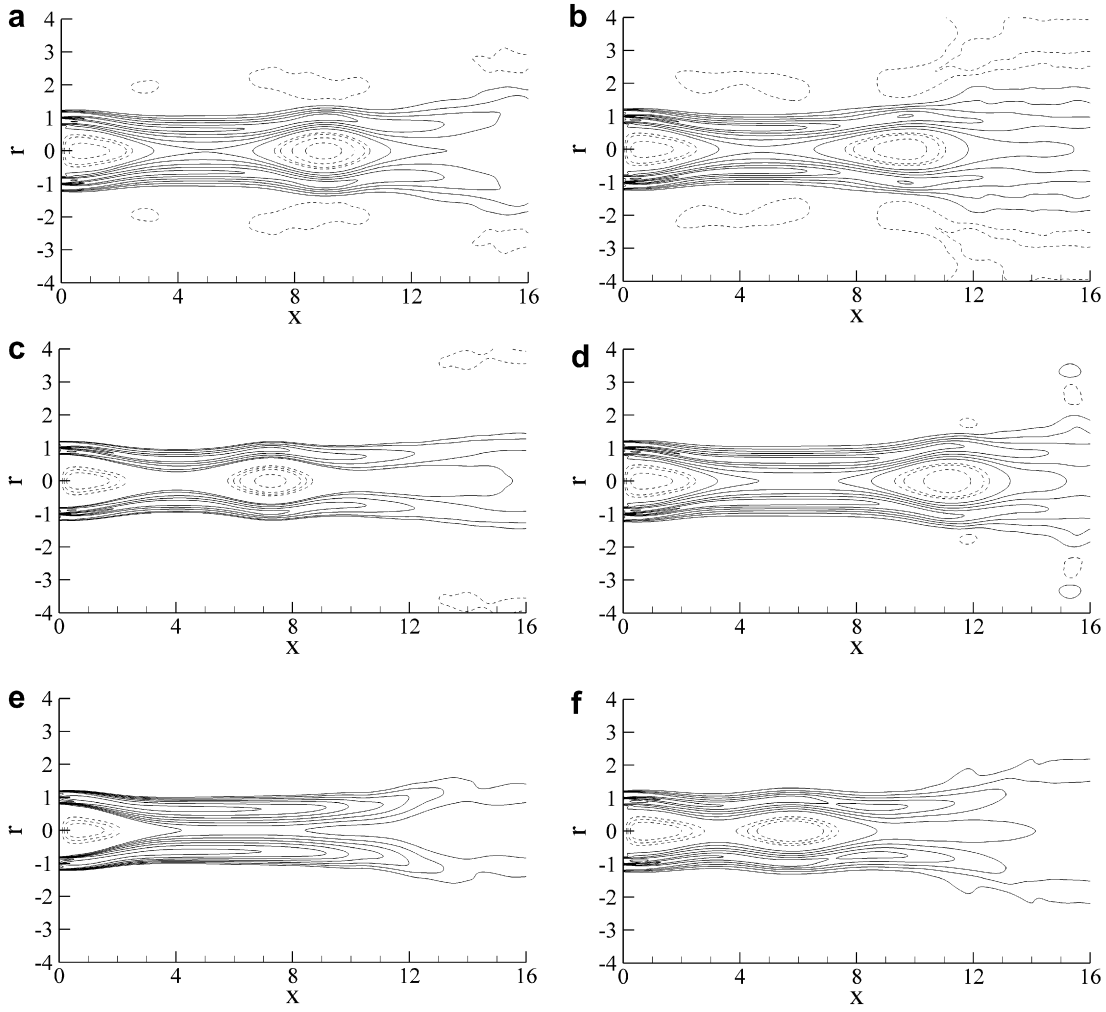

Fig. 10. Time-averaged streamwise velocity contours (solid line: positive; dashed line: negative).

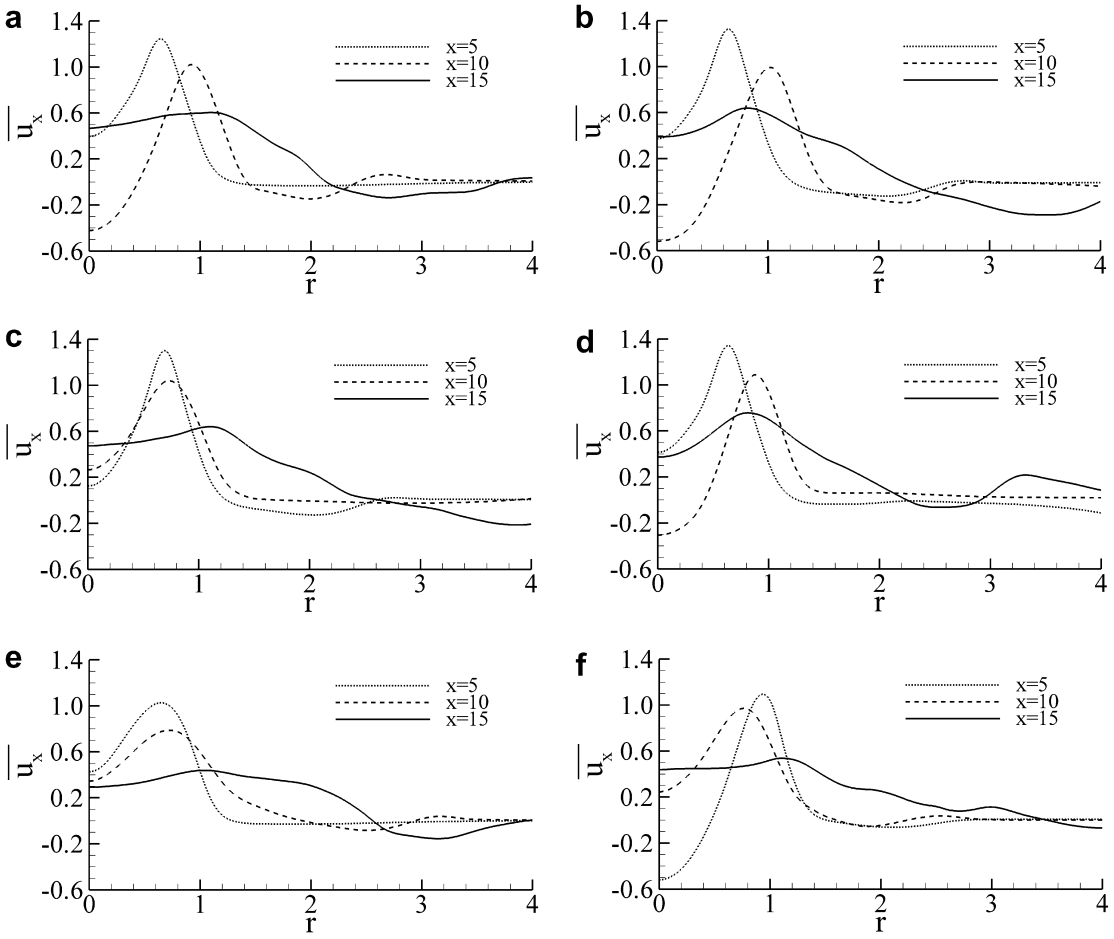

Fig. 11. Time-averaged streamwise velocity profiles at different cross-streamwise locations.

5. Concluding remarks

A computational study of annular liquid jets in compressible gas environments by direct solution of the Navier–Stokes equations has been carried out. An Eulerian approach with mixed-fluid treatment has been utilised in the mathematical formulation of the gas–liquid two-phase flow system, where the gas phase has been treated as fully compressible. An adaptation of the VOF method to accommodate the compressible gas phase has been presented. The governing equations have been directly solved using highly accurate numerical methods. Six idealised axisymmetric cases have been numerically analysed, in order to examine the effects of surface tension, liquid sheet thickness, density ratio and viscosity ratio on the flow development.

The simulations have shown that the annular jet flow is characterised by a recirculation zone adjacent to the nozzle exit. The annular liquid jet showed the well known "bell shape" before the collapse of liquid sheets at further downstream locations where large-scale vortical structures are formed due to the Kelvin–Helmholtz instability. The increased liquid sheet thickness showed an increase in the dispersion of the liquid in the compressible gas medium. The presence of surface tension tends to promote the development of the instability and the development of vortical structures. The non-existence of surface tension results in smaller liquid dispersion. A reduction in the liquid-to-gas density ratio resulted in a more stable flow field while a reduced liquid-to-gas viscosity ratio increased the instability and thus increased the liquid dispersion.

This study is an effort towards a full three-dimensional (3D) spatial DNS of annular liquid jets involving flow swirling and the formation of large and small liquid droplets, which is currently underway. The 3D spatial DNS will be able to capture the fine details of liquid disintegration and breakup, which are difficult to capture in idealised axisymmetric simulations due to a lack of three-dimensional vortex stretching and interaction. A full 3D spatial DNS can also provide useful databases for the development of physical models of liquid breakup and atomization.

References

Adzic, M., Carvalho, I.S., Heitor, M.V., 2001. Visualisation of the disintegration of an annular liquid sheet in a coaxial airblast injector at low atomising air velocities. Opt. Diagnost. Eng. 5, 27–38.

Albina, F., Peric, M., 2000. Numerical simulation of spray instabilities. In: Proceedings of the 16th Annual Conference on Liquid Atomisation and Spray Systems. CD-ROM, ILASS-Europe 16.

Banerjee, S., Lakehal, D., Fulgosi, M., 2004. Surface divergence models for scalar exchange between turbulent streams. Int. J. Multiphase Flow 30, 963–977.

Brackbill, J.U., Kothe, D.B., Zemach, C., 1992. A continuum method for modelling surface tension. J. Comput. Phys. 100, 335–354.

Cao, J., 2003. Theoretical and experimental study of atomization from an annular liquid sheet. Proceedings of the Institution of Mechanical Engineers Part D. J. Automobile Eng. 217, 735–743.

Choi, C.J., Lee, S.Y., 2005. Droplet formation from a thin hollow liquid jet with a core air flow. Atomizat. Spray 15, 469–487.

Crowe, C.T., 2006. Multiphase Flow Handbook. Taylor & Francis, Boca Raton.

De Villiers, E., Gosman, A.D., Weller, H.G., 2004. Large eddy simulation of primary diesel atomisation. SAE 2004-01-0100.

Del Taglia, C., Blum, L., Gass, J., Ventikos, Y., Poulikakos, D., 2004. Numerical and experimental investigation of an annular jet flow with large blockage. J. Fluid Eng. 126, 375–384.

Fulgosi, M., Lakehal, D., Banerjee, S., DeAngelis, V., 2003. Direct numerical simulation of turbulence in a sheared air–water flow with a deformable interface. J. Fluid Mech. 482, 319–345.

Gao, D., Morley, N.B., Dhir, V., 2003. Numerical simulation of wavy falling film flow using VOF method. J. Computat. Phys. 192, 624–642.

Gueyffier, D., Li, J., Nadim, A., Scardovelli, R., Zaleski, S., 1999. Volume-of-fluid interface tracking with smoothed surface stress methods for three-dimensional flows. J. Computat. Phys. 152, 423–456.

Hirt, C.W., Nichols, B.D., 1979. Volume of fluid (VOF) method for the dynamics of free boundaries. J. Computat. Phys. 39, 201–225.

Hou, T.Y., Lowengrub, J.S., Shelley, M.J., 2001. Boundary integral methods for multicomponent fluids and multiphase materials. J. Computat. Phys. 169, 302–362.

Ibrahim, E.A., McKinney, T.R., 2006. Injection characteristics of non-swirling and swirling annular liquid sheets. Proceedings of the Institution of Mechanical Engineers Part C. J. Mech. Eng. Sci. 220, 203–214.

Jiang, X., Avital, E.J., Luo, K.H., 2004a. Sound generation by vortex pairing in subsonic axisymmetric jets. AIAA J. 42, 241–248.

Jiang, X., Luo, K.H., 2000. Direct numerical simulation of the puffing phenomenon of an axisymmetric thermal plume. Theor. Comp. Fluid Dyn. 14, 55–74.

Jiang, X., Zhao, H., Cao, L., 2004b. Direct computation of a heated axisymmetric pulsating jet. Numer. Heat Transfer Part A 46, 957–979.

Klein, M., 2005. Direct numerical simulation of a spatially developing water sheet at moderate Reynolds number. Int. J. Heat Fluid Flow 26, 722–731.

Lasheras, J.C., Villermaux, E., Hopfinger, E.J., 1998. Break-up and atomization of a round water jet by a high-speed annular air jet. J. Fluid Mech. 357, 351–379.

Leboissetier, A., Zaleski, S., 2001. Direct numerical simulation of the atomisation of a diesel jet. In: Proceedings of the 17th Annual Conference on Liquid Atomisation and Spray Systems. CD-ROM, ILASS-Europe 17.

Lele, S.K., 1992. Compact finite-difference schemes with spectral-like resolution. J. Computat. Phys. 103, 16–42.

Lin, S.P., 2003. Breakup of Liquid Sheets and Jets. Cambridge University Press, Cambridge.

Lin, S.P., Reitz, R.D., 1998. Drop and spray formation from a liquid jet. Annu. Rev. Fluid Mech. 30, 85–105.

Lombardi, P., DeAngelis, V., Banerjee, S., 1995. Direct numerical simulation of near-interface turbulence in coupled gas–liquid flow. Phys. Fluid 8, 1643–1665.

Lozano, A., Barreras, F., Hauke, G., Dopazo, C., 2001. Longitudinal instabilities in an air-blasted liquid sheet. J. Fluid Mech. 437, 143–173.

Lozano, A., Barreras, F., Siegler, C., Löw, D., 2005. The effects of sheet thickness on the oscillation of an air-blasted liquid sheet. Exp. Fluid 39, 127–139.

Luo, K.H., Sandham, N.D., 1997. Direct numerical simulation of supersonic jet flow. J. Eng. Math. 32, 121–142.

Mehring, C., Sirignano, W.A., 2000. Axisymmetric capillary waves on thin liquid sheets. II. Spatial development. Phys. Fluid 12, 1440–1460.

Michalke, A., 1984. Survey on jet instability theory. Prog. Aerospace Sci. 21, 159–199.

Mitchell, B.E., Lele, S.K., Moin, P., 1999. Direct computation of the sound generated by vortex pairing in an axisymmetric jet. J. Fluid Mech. 383, 113–142.

Nie, Q., 2001. The nonlinear evolution of vortex sheets with surface tension in axisymmetric flows. J. Computat. Phys. 174, 438–459.

Perry, R.H., Green, D.W., 1998. Perry's Chemical Engineers' Handbook. McGraw-Hill, Singapore.

Poinsot, T.J., Lele, S.K., 1992. Boundary conditions for direct simulations of compressible viscous flows. J. Computat. Phys. 101, 104–129.

Ramamurthi, K., Tharakan, T.J., 1998. Flow transition in swirled liquid sheets. AIAA J. 36, 420–427.

Rangel, R.H., Sirignano, W.A., 1988. Nonlinear growth of Kelvin–Helmholtz instability: effect of surface tension and density ratio. Phys. Fluid 31, 1845–1855.

Rangel, R.H., Sirignano, W.A., 1991. The linear and nonlinear shear instability of a fluid sheet. Phys. Fluid A 3, 2392–2400.

Richards, J., Lenhoff, A.B.A., 1995. Drop formation in liquid–liquid systems before and after jetting. Phys. Fluid 7, 2617–2630.

Sheen, H.J., Chen, W.J., Jeng, S.Y., 1996. Recirculation zones of unconfined and confined annular swirling jets. AIAA J. 34, 572–579.

Shen, J., Li, X., 1995. Breakup of annular viscous liquid jets in two gas streams. J. Propul. Power 12, 752–759.

Shen, J., Li, X., 1996. Instability of an annular viscous liquid jet. Acta Mech. 114, 167–183.

Sirignano, W.A., Mehring, C., 2000. Review of theory of distortion and disintegration of liquid streams. Prog. Energy Combust. Sci. 26, 609–655.

Stiesch, G., 2003. Modeling Engine Spray and Combustion Processes. Springer, Berlin.

Thompson, K.W., 1987. Time dependent boundary conditions for hyperbolic systems. J. Computat. Phys. 68, 1–24.

Williamson, J.H., 1980. Low-storage Runge–Kutta schemes. J. Computat. Phys. 35, 1–24.

Wray, A.A., 1986. Very low storage time-advancement schemes. Internal Report, NASA-Ames Research Center, Moffett Field, California.

Zhang, R., He, X., Doolen, G., Chen, S., 2001. Surface tension effects on two-dimensional two-phase Kelvin–Helmholtz instabilities. Adv. Water Res. 24, 461–478.